www.elsevier.com/locate/jmps

The effect of size, orientation and alloying on the deformation of AZ31 nanopillars

Zachary H. Aitken, Haidong Fan, Jaafar A. El-Awady, Julia R. Greer

PII: S0022-5096(14)00238-5
DOI: http://dx.doi.org/10.1016/j.jmps.2014.11.014
Reference: MPS2565

To appear in: *Journal of the Mechanics and Physics of Solids*

Received date: 14 May 2014
Revised date: 14 October 2014
Accepted date: 30 November 2014

Cite this article as: Zachary H. Aitken, Haidong Fan, Jaafar A. El-Awady and Julia R. Greer, The effect of size, orientation and alloying on the deformation of AZ31 nanopillars, *Journal of the Mechanics and Physics of Solids,* http://dx.doi.org/10.1016/j.jmps.2014.11.014

The Effect of Size, Orientation and Alloying on the Deformation of AZ31 Nanopillars

Zachary H. Aitken[a,], Haidong Fan[b,c], and Jaafar A. El-Awady[b] Julia R. Greer[d]*

[a] Department of Mechanical and Civil Engineering, California Institute of Technology Pasadena, CA 91125, United States, *Email: zaitken@caltech.edu , Phone: 626-395-4416.

[b] Department of Mechanical Engineering, Johns Hopkins University Baltimore, Maryland 21218, United States
[c] Department of Mechanics, Sichuan University, Chengdu, Sichuan 610065, China
[d] Division of Engineering and Applied Science, California Institute of Technology Pasadena, CA 91125, United States

Abstract

We conducted uniaxial compression of single crystalline Mg alloy, AZ31 (Al 3% wt. and Zn 1% wt.) nanopillars with diameters between 300-5000 nm with two distinct crystallographic orientations: (1) along the [0001] c-axis and (2) at an acute angle away from the c-axis, nominally oriented for basal slip. We observe single slip deformation for sub-micron samples nominally oriented for basal slip with the deformation commencing via a single set of parallel shear offsets. Samples compressed along the c-axis display an increase in yield strength compared to basal samples as well as significant hardening with the deformation being mostly homogeneous. We find that the "smaller is stronger" size effect in single crystals dominates any improvement in strength that may have arisen from solid solution strengthening. We employ 3D-discrete dislocation dynamics (DDD) to simulate compression along the [0001] and $[1122]$ directions to elucidate the mechanisms of slip and evolution of dislocation microstructure. These simulations show qualitatively similar stress strain signatures to the experimentally obtained stress-strain data. Simulations of compression parallel to the $[1122]$ direction reveal the activation and motion of only <a>-type dislocations and virtually no dislocation junction formation. Computations of compression along [0001] show the activation and motion of both <c+a> and <a> dislocations along with a significant increase in the formation of junctions corresponding to the interaction of intersecting pyramidal planes. Both experiments and simulation show a size effect, with a differing exponent for basal and pyramidal slip. We postulate that this anisotropy in size effect is a result of the underlying anisotropic material properties only. We discuss these findings in the context of the effective resolved shear stress relative to the unit Burgers vector for each type of slip, which reveal that the mechanism that governs size effect in this Mg-alloy is equivalent in both orientations.

Keywords: Nano-Compression Experiments; Discrete dislocation dynamics; Magnesium; Orientation effects; Size effects.

1. Introduction

There has been an increasing demand for lightweight materials in the automotive and aerospace industries, which resulted in renewed surge of interest in Mg and its alloys. As early as the 1920's Mg-alloys were utilized in airplane engines and racecar components [1,2] for their light weight and favorable strength [3–6]. In addition to being the lightest structural metal, Mg has been shown to exhibit excellent fatigue resistance [7] and high damping capacity [8], but its poor formability and limited ductility has prevented the development of production processes for component parts. This low ductility at room temperature is caused by the inherent anisotropy and a shortage of available slip systems in hexagonal close-packed (HCP) materials. For pure Mg at room temperature, dislocation slip in the basal crystallographic planes is the dominant deformation mechanism. This provides only two independent slip systems for deformation; whereas five are required to carry out homogeneous deformation, as specified by the von Mises criteria [9].

Several methods have been pursued to improve the ductility of Mg, for example alloying and texture control [10–12]. For The mechanisms that lead to enhanced ductility in the alloys are thought to be an elevated activity of non-basal slip systems through a decrease in the Peierls stress, but the evidence of such easing of non-basal slip in single crystalline alloys has been limited to prismatic slip in tension of a small selection of binary alloys [11]. Developing a thorough understanding of the mechanical properties and deformation mechanisms in Mg and its alloys is of fundamental importance. Of particular interest are alloys utilizing Al and Zn, designated by convention as the "AZ" alloys, with the subsequent number referring to the weight percent of the alloying elements. A lack of experimental data, which describes deformation of single-crystalline AZ31 (3% wt. Al, 1% wt. Zn) alloy, including the elastic moduli and the critical resolved shear stresses, as well as an understanding of the underlying dislocation mechanisms presents an impediment to help guide the development of improved Mg alloys. In part, such a shortage of data stems from the lack of availability of single crystals of AZ31 able to be used in conventional macro-scale mechanical testing. Hot rolling and extrusion are the preferred processing method because of the resulting fine-grained microstructure.

The grain size in a typical AZ alloy after extrusion can vary between 2 and 23 μm depending on extrusion conditions [13,14]. Nano-scale uniaxial compression experiments then offer a useful methodology to test single-crystalline Mg alloy samples in a variety of known crystallographic orientations. The anisotropy of the slip systems and challenges associated with sample preparation have rendered HCP crystals a less explored material system for nano-plasticity testing in contrast to face-centered cubic and body-centered cubic metals, for example. Mg is also known to deform via twinning which can make the mechanical response difficult to interpret. A key finding in virtually all uniaxial compression studies on micro and nano-sized single crystalline metals is the emergent dependence of the flow stress on sample dimensions,

with smaller generally being stronger for single crystals [15,16]. Face-centered and body-centered cubic materials follow a power law scaling behavior, with an average exponent of –0.6 for FCC materials. It should be noted that the exponent is also a strong function of the initial dislocation density [17,18]. Recently, attention has been directed towards identifying the effect of crystal size and orientation on the deformation mechanisms and mechanical properties of pure Mg microcrystals [19–24] using the micro-tension and/or micro-compression experimental technique [25]. Hexagonal close-packed materials also appear to follow a scaling law, but with a lack of data the scaling behavior is less clear [16]. Clearly, further investigation is required into the nano-scale mechanical behavior of HCP metals to reach the same level of understanding we have of cubic metals.

Byer et al. performed uniaxial compression experiments on micron-sized Mg single crystals where the loading direction was parallel to the c-axis of the crystal [19]. These single crystals were fabricated in a cylindrical geometry with diameters ranging between 2.5-10 µm. The authors reported the activation of the pyramidal slip planes and significant hardening under compression up to 12% strain. No deformation twinning was observed. Across the sample sizes of 2.5 to 10 microns utilized in this study, virtually no size effects were observed, which was hypothesized to stem from the very high dislocation densities present in these crystals. The same authors investigated the effect of initial dislocation density of the mechanical behavior of single crystalline Mg pillars, whereby samples with diameters of 600 nm - 10 µm were prepared and uniaxially compressed along [0001] and $[2\bar{3}\bar{1}4]$ axis [22]. The initial dislocation density was controlled by fabricating compression pillars from samples that contained a deformation layer introduced during mechanical polishing prior to fabrication and from samples where this deformed layer was etched away. Pyramidal slip was reported for samples compressed parallel to the c-axis, with no deformation twinning. Basal slip was the preferred deformation mechanism for samples compressed along the $[2\bar{3}\bar{1}4]$ axis. A power-law size effect was observed in the samples with a low initial dislocation density of (1.1±0.18) x 10^{13} m^{-2} in both orientations, which was suppressed when the dislocation density was increased to (3.0±0.5) x 10^{13} m^{-2}. Lilleoden also performed micro-compression tests along the (0001) axis of single crystalline Mg micropillars with diameters ranging between 2.1 to 10 µm [20]. A size effect and pyramidal slip with no deformation twinning was reported.

On the other hand, Ye, et al. conducted uniaxial compression experiments on pure Mg and Mg-0.2% Ce alloy in an in-situ TEM [21]. These authors observed a significant size effect for samples with diameters between 200 nm to 1.6 µm in all tested orientations. When compressed along the [3-94] axis, basal slip dominated deformation. In contrast to previous reports, extension twinning was reported in both Mg and Mg-0.2% Ce when deformed along the [0001] axis. A decrease to 15% of the critical resolved shear stress of pure Mg was reported for Mg-0.2% Ce alloy samples.

Following this work, Yu, et al. performed in-situ TEM compression, tension, and bending experiments such that the [0001] direction was always parallel to the loading direction[25]. Samples were square in cross-section, with side lengths of 150 nm. The nucleation and growth of a single contraction twin was observed in compression, while an array of nano-twins was formed as a result of tension along the same axis.

Kim performed uniaxial compression on pure Mg parallel to the [0001], $[2112]$, $[10\bar{1}1]$, $[11\bar{2}0]$ and $[10\bar{1}0]$ directions [23,24]. Single crystal samples varied in diameter between 1 to 10 µm. Compression parallel to the [0001], $[2112]$ and $[10\bar{1}1]$ axes resulted in deformation by dislocation slip. In contrast, deformation twinning and dislocation slip during compression along the $[11\bar{2}0]$ and $[10\bar{1}0]$ directions was observed. The flow stress in [0001], $[2112]$, $[11\bar{2}0]$ and $[10\bar{1}0]$-oriented samples was observed to follow a power-law increase with decreasing pillar diameter. The power-law exponent was also seen to depend on the sample orientation with twinning dominated orientations showing larger exponent amplitudes.

This review of the existing experimental data on deformation of small-scale Mg and Mg-alloys can be summarized as follows:

(1) Virtually all existing reports focused on pure Mg, with the most common experiment being uniaxial compression along the c-axis.
(2) A wide range of phenomena have been reported, especially pertaining to deformation twinning, with no unified understanding on slip vs. twinning.
(3) The size-strength dependence was reported to vary among authors and orientations, but the influence of orientation on the size effect remains unresolved.

This summary demonstrates that the current understanding of small-scale deformation of Mg and Mg-alloys is incomplete and results remain inconclusive. Systematic investigations are necessary, particularly on the effect of orientation and alloying.

We present a set of systematic uniaxial compression experiments and microstructural characterization of single crystalline AZ31 alloy (Mg-3.0% Al-1.0% Zn) on small-scale cylindrical samples with diameters ranging between 300-5000 nm. We performed compressions along two distinct families of expected deformation mechanisms: (1) along [0001], which is expected to deform via pyramidal slip or compression twinning and (2) along multiple planes misoriented from the c-axis by 22-69°, which are expected to deform via basal slip.

We also employed three-dimensional (3D) discrete dislocation dynamics (DDD) simulations to identify the dislocation mechanisms controlling the size-affect response of Mg microcrystals and to further investigate their orientation dependence. All 3D-DDD simulations in this study were performed using the Multi-scale Dislocation Dynamics Plasticity (MDDP) code originally

developed by Zbib et al. [26,27] to model dislocation glide in FCC single crystals. Simulations were performed on samples with the compression axis parallel to the [0001] and $[11\bar{2}2]$ crystallographic directions; orientations expected to deform by pyramidal and basal slip, respectively.

Experimentally we observed two distinct stress-strain signatures and deformation characteristics with no observable deformation twinning. 3D-DDD simulations showed a dependence of stress-strain signature and attained stresses on orientation that is in qualitative agreement with experiments. A unique size effect was present in each crystallographic orientation in both experiments and simulations, each following the "smaller is stronger" trend. We show that the mechanism controlling the size effect in both orientations is the activation of the weakest source and that the anisotropy in intrinsic lattice resistance gives rise to a difference in scaling exponents. This implies that in the AZ31 alloy, the deformation at the submicron length-scale is dominated by the size effect rather than by solid solution strengthening through alloying. We discuss these findings in the framework of small-scale plasticity and crystallographic slip mechanisms.

2. Methods

2.1. Compression Experiments

Bulk samples of AZ31 were first prepared from wrought alloys using equal channel angular extrusion (ECAE) following route $4B_C$. This process involved extruding the material through a 90° angular channel a total of 4 passes, rotating the billet 90° about its axis after each extrusion at 200 °C and 1240 psi. Several smaller cubic pieces of 1 cm^3 were then extracted using electron discharge machining (EDM).

A chosen surface of one of the cubic AZ31 blocks was then mechanically polished using abrasive lapping pads embedded with aluminum oxide (Al_2O_3) particles. Pads with successively finer particle sizes were used to polish the surface down to a final 3 μm particle size.

Mechanical polishing was followed by electrolytic polishing in a solution of ethanol and phosphoric acid (85%) in a volume ratio of 5:3. A polishing mask was used to expose an area of 0.25 cm^2 of the metal surface to the electrolyte. Electro-polishing was performed using a voltage of 2V, and the polishing solution was maintained at a temperature between 0-5 °C throughout the process. After polishing for 2-3 minutes, the sample was immediately removed from the polishing table and immersed in methanol. Gentle agitation followed by sonic cleaning fully dissolved the white film that formed on the surface during polishing. The sample was then allowed to dry in air and typically yielded a mirror finish. Figure 1b shows a SEM image of the polished surface. Polishing at higher temperatures, for longer times, or failure to immediately immerse in methanol always resulted in the formation of a dull, porous surface oxide layer.

Figure 1a shows a TEM micrograph of this surface layer. Energy dispersive spectroscopy (EDS) data shows a high concentration of phosphorous from the electrolyte localized in this layer. The thickness and surface coverage of this oxide appeared to increase with temperature and polishing time. This surface oxide could be removed using a buffered hydrofluoric acid etch and yielded a smooth surface, but the surface quality degraded after 2-3 days.

Electron backscatter diffraction (EBSD) was used to characterize the size and orientation of grains. Presence of a surface oxide layer from poor sample preparation resulted in an inability to obtain a clear Kikuchi pattern from the bulk. Figure 1c shows an Orientation Imagining Microscopy (OIM) crystallographic map generated based on the polished surface after a thermal anneal in vacuum at 450° C for 5 hours. Processing using Oxford's Channel 5 software revealed a strong basal texture ~80° from the extrusion direction and an average grain size of 2.5±1.6 μm before thermal annealing. This grain size is consistent with other reports for AZ31 processed via ECAE under similar conditions [14], but is too small to guarantee that the compression samples fabricated using the FIB will be single crystalline. Thermal annealing at 450° C for 5 hours increased the average grain size to 11.5±9.6 μm [28].

Cylindrical compression samples were fabricated using Focused Ion Beam (FIB) and the top-down methodology [29–33]. The specific grains for sample extraction were chosen such that the surface was parallel to one of two crystallographic orientations: (0001) or tilted acutely away from the c-axis. Figure 1d shows a stereographic triangle and gives the orientations of the grains used to fabricate compression samples. The fabrication was accomplished by placing concentric annular patterns into the field of view on the ion-beam image and progressively milling away material until the final inner pattern diameter of 300-5000 nm. The aspect ratio, height/diameter, was maintained between 3:1 and 4:1. Sample diameters were calculated by taking the average of the diameter measured at the top of the pillar height and the bottom of the pillar height. A SEM image of a representative single-crystalline sample after deformation is shown in Figure 2b.

Uniaxial compression experiments were performed in a nanoindenter (Triboscope, Hysitron Inc.) using a diamond flat punch tip with a diameter of 8 μm. Tests were conducted under displacement rate control, at the nominal strain rate of 10^{-3} s^{-1} up to a total strain between 8-15%. The displacement was monitored continuously at a frequency of 78 kHz via a feedback loop through the Hysitron *performec* control module. Engineering stress and strain were calculated by dividing the force and displacement by the initial cross-sectional area and pillar height, respectively. Resolved shear stresses were determined using the maximum Schmid factor for each slip system calculated from the crystal orientation obtained from OIM analysis. Bunge Euler angles $\{\phi_1, \theta, \phi_2\}$ were first converted to their corresponding Miller-Bravais [hkil] direction values using [34]:

$$\begin{bmatrix} h \\ k \\ i \\ l \end{bmatrix} = \begin{bmatrix} \frac{\sqrt{3}}{2} & -\frac{1}{2} & 0 \\ 0 & 1 & 0 \\ -\frac{\sqrt{3}}{2} & -\frac{1}{2} & 0 \\ 0 & 0 & \frac{c}{a} \end{bmatrix} \begin{bmatrix} \sin\varphi_2 \sin\theta \\ \cos\varphi_2 \sin\theta \\ \cos\theta \end{bmatrix} \quad \text{Eq. (1)}$$

Where $\frac{c}{a}$ is the ratio between the length of the c-axis and the in-plane lattice constant within the unit cell and is 1.624 for Mg. The vector on the right hand side of Eq. 1 corresponds to the z-component of a Bunge rotation of an orthonormal coordinate system and the matrix transforms the orthonormal system to the Miller-Bravais basis. The 4-index Miller-Bravais notation of a given deformation system, {*hkil*}/<*uvtw*>, can be converted to 3-index hexagonal Miller notation by [35]:

$$h_1 \quad k_1 \quad l_1 \;=\; h-i \quad k-i \quad \frac{3}{2}\left(\frac{a}{c}\right)^2 l \quad \text{Eq. (2)}$$

$$u_1 \quad v_1 \quad w_1 \;=\; u-t \quad v-t \quad w \quad \text{Eq. (3)}$$

Note that in the hexagonal system a direction is not necessarily normal to a plane of the same indices and so the deformation plane must first be converted to its corresponding direction normal as seen in Eq. (2). The direction cosine between the loading direction and the deformation plane normal direction, $cos\varphi$, and the direction cosine between the loading direction and the slip direction, $cos\lambda$ are calculated as:

$$\cos\ \varphi \text{ or } \lambda = \frac{u_1u_2+v_1v_2-\frac{1}{2}\left(u_1v_2+u_2v_1\right)+\left(\frac{c}{a}\right)^2 w_1w_2}{\sqrt{u_1^2+v_1^2-u_1v_1+\left(\frac{c}{a}\right)^2 w_1^2}\ \sqrt{u_2^2+v_2^2-u_2v_2+\left(\frac{c}{a}\right)^2 w_2^2}} \quad \text{Eq. (4)}$$

Where $u_2 \quad v_2 \quad w_2$ is the loading direction and $u_1 \quad v_1 \quad w_1$ is the deformation plane normal direction (or the deformation direction). The Schmid factor, M, then has the common meaning of:

$$M = cos\varphi cos\lambda \quad \text{Eq. (5)}$$

Yield stresses were determined by the stress at the first significant strain burst event. This event can be identified by a sudden increase in the velocity of the indenter tip that results in a discontinuity in the data. This increase varied among samples, but was typically 4-5 standard deviations above the average tip velocity. If no bursts were present in the data, a 0.2% offset

method was utilized with a slope approximated from a region on the loading curve after the initial non-linear segment when the tip is not in full contact with the pillar head.

Analysis of microstructure in the polished material and deformed samples was performed via transmission electron microscopy (TEM) (FEI, Tecnai F30) at an accelerating voltage of 300 kV. Samples were lifted out from the bulk polycrystal using a micro-manipulator within the FIB (Omniprobe, Inc.) and attached to a TEM grid with ion-beam assisted, site-specific, Pt deposition. Once attached to the TEM grid, the samples were thinned using decreasing current down to 10 pA, to a thickness of <100 nm to ensure electron transparency.

2.2. Discrete Dislocation Dynamics Simulations

To allow for the simulations of dislocation ensembles in HCP microcrystals, the slip planes and Burgers vectors of the HCP lattice (summarized in Table 1 [36]) were introduced into MDDP. The experimentally measured Peierls stresses for dislocations on the basal, prismatic, and pyramidal planes, which equal 0.52 [37], 39.2 [38] and 105 MPa [39], respectively, were introduced into the code. These values also agree with molecular dynamics (MD) simulations on these slip systems [40,41]. Since cross-slip in HCP crystals is not yet fully characterized in literature, the current simulations did not consider this possible deformation mechanism. Two orientations were simulated, namely, microcrystals oriented for compression along the *c*-axis $[0001]$, and along the $[1122]$ directions. In the 1122 orientation, the *c*-axis makes an angle of 45° with respect to the loading axis.

All simulated microcrystals had a rectangular shape with a squared cross-section having an edge length, *D*, varying between 0.5 and 1.0 μm, and a fixed aspect ratio of h/D = 2.5. The microcrystal bottom surface was constrained in all directions (i.e. $u_x = u_y = u_z = 0$), and a displacement-controlled compressive load was applied on the top surface such that $u_z = \varepsilon h$ [42]. The nominal strain rate was fixed in all simulations at $\dot{\varepsilon} = 1000s^{-1}$, which is higher than that in experiments to reduce the computation cost [42]. The drag coefficient for pure screw dislocations was set to $B_{screw} = 10^{-1}$ Pa s, and for non-screw dislocations $B_{non\text{-}screw} = 10^{-4}$ Pa s [43]. The initial dislocation density in all simulations was $\rho_{src} = 6\times10^{12}$ m^{-2}, with a random dislocation length, l_{src}, between 0.19-0.32 μm (i.e. mean length is 800*b*). 8 realizations for each microcrystal size and orientation with different initial random dislocation distributions were simulated. To account for the anisotropy of the HCP lattice, the shear modulus along the *c*-axis was 22.4 GPa, along the basal slip is 12.7 GPa, and the Poisson ratio is ν = 0.34 [23]. Finally, the mass density 1738 kg/m^3, the Burgers vector magnitude for <*a*> dislocations was *b* = 0.32 nm, and the c/a ratio = 1.624, were all inputs to the DDD simulations.

From the current experiments, as well as others published in literature, dislocation-mediated plasticity was observed to be the dominant deformation mechanism in micron and submicron crystals, and no twinning has been observed [19–23]. However, for microcrystals having sizes below 250 nm, twining reoccurs under *c*-axis compression loading [25]. Hence, the DDD simulations performed here, which account only for dislocation evolution, can effectively model the deformation mechanisms in microcrystals larger than 250 nm. In addition, we have performed preliminary simulations with dislocations on all four slip planes, however, only $\langle a \rangle$-dislocations on basal planes (i.e. $(0001)< 1120 >$), and $\langle c+a \rangle$-dislocations on 2nd order pyramidal planes (i.e. $(1122) < 1123 >$) play the major role in either orientation. Furthermore, recent MD simulations also shows that <c+a>-dislocations nucleate on 1st order pyramidal planes then transition to 2nd order pyramidal planes through cross-slip or cooperative slip. Consequently, slip would subsequently occur predominantly on 2nd order pyramidal planes [44]. This agrees well with reports that only basal and 2nd order pyramidal slip were observed experimentally for both orientations [19–23]. Thus, in the following simulations, only these two types of dislocations were considered. The initial dislocation density prescribed on basal planes was 4×10^{12} m^{-2}, and on 2nd order pyramidal planes was 2×10^{12} m^{-2}.

A small degree of misorientaion (<10°) was typically reported for microcrystals oriented for *c*-axis compression [22,23]. This misorientaion is either pre-existent or develops during deformation due to crystallographic rotation resulting from a stiff loading axis that produces high friction forces between the microcrystal top-surface and the load platen [45,46]. To mimic this frictional stress effect, an increasing shear stress is applied on the top surface in the $[0001]$ case. This shear stress is expressed as $\tau_{top} = \tau_{zx} = |\sigma| \tan(\theta_{mis})$, where σ is the applied axial stress, $\theta_{mis} = 10° (\varepsilon - \varepsilon_y)/(\varepsilon_{final} - \varepsilon_y)$ for $\varepsilon > \varepsilon_y$ is the misorientation angle, ε_y is the yielding strain, ε_{final} is the final strain of 1.5%. Thus, the maximum misorientation angle will be 10° at the end of the simulations.

3. Results

We report the results of compression experiments binned by similar diameter and compare the data across all tested orientations. Each stress-strain curve is representative for a given orientation and displays qualitative features common to each pillar within the set.

3.1. Basal Slip Orientation: 22-69° tilted from {0001}

A SEM image of a representative sample with the diameter of 847 nm is shown in Figure 2b. The stress-strain data shown in Figure 2a exhibits several strain bursts typical of single crystalline micro-and nano-scale pillar compression tests [15,16]. The axial flow stress at the unloading strain of 16% is 107 MPa, which shows that negligible strain hardening occurred between yield at 115 MPa and unloading. The SEM image of this sample after the compression

is shown in Figure 2b and reveals that the deformation commenced by a series of parallel shear offsets emanating from the top of the pillar.

In contrast, a 2125 nm-diameter sample yielded at 34 MPa and showed an increase in stress up to 86 MPa at the final unloading strain of 10%. The post-deformation image given in Figure 2c indicates that deformation was accommodated by a series of parallel shear offsets along the pillar.

An inclination of 48° between the loading direction and the c-axis in the 847 nm diameter sample shown in Figures 2b, results in a critical resolved shear stress (CRSS), τ_{CRSS}, of 51 MPa; an inclination of 22° in the 2125 nm-diameter sample results in a CRSS of 11 MPa. These values are comparable to the range of CRSS of 39-68 MPa reported for the 3 μm diameter Mg single crystals compressed along the $[2314]$ direction [22]. For the 847 nm-diameter AZ31 sample studied in this work this represents an increase in CRSS by two orders of magnitude over the basal CRSS of Mg (~0.5 MPa) and 29 times the basal CRSS of Mg+0.45 at.% Zn (1.75 MPa) bulk single crystals [10,37]. The average elastic modulus was estimated to be 40.5±9.2 GPa and compares well to the average modulus of pure Mg (43.7 GPa) [47] and Mg + 4.5% Al + 1% Zn (44.6 GPa) [48] at similar tilt angles between 22-69° from the c-axis.

3.2. Pyramidal Slip Orientation: (0001)

The stress-strain data for a representative 840 nm-diameter pillar oriented for pyramidal slip is shown in Figure 3b. This sample yielded at an axial stress of 654 MPa, and the stress-strain data displayed similar strain bursts characteristic to basal slip-oriented samples shown in Figure 2a. The final stress at the unloading strain of 11.6% was 831 MPa, a value 27% higher than the yield stress. Figure 3c shows a SEM image of this sample after compression and reveals that the deformation was mostly homogeneous. The sample diameter widened from 840 nm to 940 nm and barreled. A small shear offset at midpoint of the cylinder oriented perpendicular to the loading axis was also observed. Micron-sized samples showed qualitatively similar stress-strain data.

The axial yield stress compares well to axial stresses of pure Mg micro-pillars with 630-685 nm diameter compressed along the c-axis of 600-680 MPa [22]. A misorientation from the c-axis of 2.2° corresponds to resolved shear stresses for 2nd order <a+c> pyramidal slip of 302 MPa. The average elastic modulus was 61.6±10.3 GPa compared to the modulus along the c-axis of 50.8 GPa in pure Mg [49].

3.3. Microstructure Analysis

Figure 4a shows a bright field TEM micrograph that reveals several rod-like and circular second phase particles with the average diameters of 29 nm. A high-resolution TEM of one of these particles is shown in Figure 4b. Energy dispersive x-ray spectroscopy data shown in Figure 4c, indicates that these phases are Mn rich, which is consistent with its dominance in the AZ31 composition at ~0.44% wt. These particles are most likely some form of Al-Mn intermetallic that has been predicted and observed in similar AZ alloys[50–52]. The precipitate areal density was estimated to 0.98% based on measuring the total area of secondary phases in the images and with spacing as great as ~675 nm. Stanford and Atwell observed a similar dispersion of particles in bulk AZ31, and Orowan hardening in tension of bulk AZ31 [51]. In compression, the authors reported insensitivity to the precipitates and pointed to the observed proliferation of twinning during compression and suggested that the volume fraction (~0.3%) of Al-Mn particles was not sufficient to impact the twinning stress.

3.4. DD Simulations

Figure 5a shows the engineering-stress versus engineering-strain response of $[0001]$ and $[1122]$ oriented microcrystals having edge-length D = 1 μm. The yield stress of the $[0001]$ oriented microcrystals is $\sigma_y \approx 270$ MPa (i.e. resolved shear stress $\tau_y = 121$MPa), while the yield stress for the $[1122]$ oriented microcrystals is $\sigma_y \approx 50$ MPa (i.e. resolved shear stress $\tau_y = 25$ MPa). Qualitatively, [0001] microcrystals display a significant increase in stress following yield compared to $[1122]$ microcrystals. In Figure 5a, the variation of junction node number with applied strain is also plotted, and shows that more junction nodes appear in the [0001] orientated microcrystals than $[1122]$ ones. The <*a*>, <*c*+*a*>, and total dislocation densities for the two orientations are shown in Figure 5b. We can see that in the $[1122]$ case, only <*a*> dislocations on the basal plane contribute to the plastic deformation. However, in the $[0001]$ microcrystals the <*c*+*a*> dislocation density increases after yield at ~0.45% strain. After 1% strain, the <*a*> dislocation density increases rapidly and exceeds the <c+*a*> dislocation density, indicating basal slip occurs. This can also be seen in Figure 6, where the effective plastic strain map and deformation shape are shown. The [0001] orientated crystals without misorientation deform via multi-slip as shown in Figure 6b. However, under the shear stress from the simulated misorientation, acute basal slip can be seen in Figure 6a, although the Schmid factor on the basal slip planes is 0. Figure 6c shows the effective strain map of the $[1122]$ microcrystal, in which single-slip is clear. These simulations agree well with the current and previous experiment observations [22,23].

4. Discussion

4.1. Basal Slip Orientation

The samples studied in this work were oriented such that the crystallographic direction parallel to the pillar axis was 22-69° away from the c-axis. This loading path applies a resolved shear stress onto the basal planes, which represent the weakest slip among Mg slip systems. Post-deformation SEM images of these samples fabricated from two separate grains, shown in Figures 2b and 2c, confirmed that the deformation was accommodated by shear on a single set of parallel slip planes. Figure 2d shows a TEM micrograph of the cross-section of one of these slip planes. The diffraction pattern shown in the inset reveals these slip planes are basal planes.

The strain bursts observed in the stress-strain signature of these samples that deformed via basal slip are similar to those in the micro- and nano-pillar compression experiments in FCC and BCC metallic single crystals. These bursts are often attributed to dislocation avalanches released from the pinning points that get activated as dislocation sources under applied stress [30,53]. Plastic deformation with a negligible change in the flow stress up to 15% axial strain suggests the deformation likely commenced on a single slip system, resulting in an “easy glide” plastic flow. Straining with little to no hardening has been observed in similar FCC micro- and nano-pillar compression experiments on samples loaded along both high and low-symmetry orientations [29,32,53,54]. In sub-micron samples, the annihilation of mobile dislocations at the free surface before they are able to multiply maintains this Stage I-like plastic behavior. In this regime, the probability of gliding dislocations interacting with one another and creating additional pinning points is lower than their propensity for annihilating at the free surface or at another existing sink. This mechanism is consistent with the observed lack of hardening and dislocation storage.

With increasing sample size, dislocations gliding in their slip planes will be increasingly more likely to encounter other dislocations or obstacles in their path before annihilation, which will cause interactions, pinning, and entanglement among them, thereby increasing dislocation density. Such dislocation multiplication can lead to back stresses and the shutdown of dislocation sources and will require a higher applied stress to propagate and to activate new, harder sources. This mechanism is consistent with a 90% increase in stress shown in Figure 2a for a 2125 nm sample. We found that all samples with diameters above 1 μm and oriented for basal slip showed this strain hardening-like behavior, a stress strain signature that has also been observed in micron-sized samples of pure Mg [20,22].

4.2. Pyramidal Slip Orientation

Compared to the samples oriented for basal slip, samples oriented for pyramidal slip attain substantially higher yield and flow stresses, as well as exhibit significant work hardening, as shown in Figure 3b. The c-axis has a high level of slip system symmetry with six 2nd order <a+c> pyramidal slip systems that have a Schmid factor of 0.447. Compression along such a high-symmetry orientation activates multiple non-parallel slip systems, which would lead to a relatively homogeneous deformation, non-localized deformation, a high degree of strain hardening, and high flow stresses, as also reported in similar experiments on pure single-crystalline Mg samples of equivalent dimensions [55,56]. SEM images of deformed samples in this study are given in Figure 3c, and reveal a 12% increase in average diameter from 840 nm to 940 nm.

Despite the activation of multiple non-parallel slip systems, the stress-strain data contains several strain bursts, similar to those observed in samples oriented for single-slip. The typical axial yield stress of 654 MPa for 840 nm diameter samples is more than twice that for basal samples. For such high axial stress, even a relatively low misalignment of 2.2° results in the maximum Schmid factor of 0.035 on the basal planes, which gives rise to the resolved basal stress of 29 MPa at unloading, on the order of critical shear stress in the samples that deformed by basal slip. A single slip plane approximately half-way down the compressed pillar height is shown in Figure 3c and conveys that it is nearly perpendicular to the c-axis, which suggests that even at low misalignment, basal slip is also activated during deformation, similar to deformation of pure Mg with low basal Schmid factors (0.035) [55]. In a small number of samples basal slip was activated and resulted in an instability, massive failure and early termination of the test (an example stress-strain plot is given in Figure S1), but the majority of samples could not have reached the high axial stresses as great as 831 MPa if basal slip was the dominant deformation mechanism. Further, for the orientations of c-axis pillars tested, the greatest Schmid factor for prismatic slip ranges between 0.002-0.013 with an associated resolved shear stress at yield between 1.35-9.35 MPa. For the reported critical resolved shear stress of prismatic slip for Mg+0.45 at.% Zn bulk single crystals of 40.2 MPa [11], it is unlikely that prismatic slip has been activated at yield. The post-yield strain must be able to accommodate the applied deformation along the c-axis which the <a> Burgers vectors of both the basal and prismatic slip systems will be unable to accommodate. The 1st and 2nd order pyramidal systems include <c+a> dislocations and are able to accommodate the imposed c-axis deformation. It is likely the activation of **multiple pyramidal slip systems** accommodated most of the deformation, and the mutual interactions of dislocations among these pyramidal systems, as well as between the pyramidal and basal planes, caused the observed work hardening.

For samples with diameters above 1 μm failure was often observed to occur by catastrophic bursts and so no comparison of the post-elastic behavior can be made to sub-micron samples.

We performed post-deformation TEM analysis of several c-axis samples and observed no clear evidence of twinning. Figure 3d shows a post-deformation TEM micrograph of a 860 nm-diameter c-axis pillar that was deformed to 4.8% engineering strain. The diffraction contrast indicates a high dislocation density and there is a lack of twinning boundaries. The inset diffraction spot pattern shows that the sample is single crystalline. This evidence along with the discussion in the previous paragraphs leads us to conclude that the dominant deformation mechanism in these samples was **via pyramidal slip**, in agreement with similar (pure Mg) micron-sized pillars compressed parallel to the c-axis [19,20,22]. These results are in contrast to the work of Yu, et al, in which pillars with diameters ranging from 150-200 nm in width with a rectangular cross-section, displayed twin nucleation and twin propagation during [0001] compression, while nano-twin arrays formed during [0001] tension [25]. Easy activation of deformation twinning was also observed in bulk AZ31 compressed along the c-axis [57]. Although Al and Zn are typically expected to decrease the stacking fault energy of Mg [58] allowing for easier activation of twinning, we found pyramidal slip to be the prevalent deformation mechanism when compressed along the c-axis.

4.3. 3D-DDD Simulations

Stress strain curves generated by 3D-DDD simulations showed several qualitative features also observed experimentally including: anisotropy in the yield stress of pillars oriented for basal or pyramidal slip, strain hardening of samples compressed along the [0001] direction, and activation of basal slip during [0001] compression with an induced misalignment.

Figure 5a shows a difference of 96 MPa between the CRSS of pillars in the $[1122]$ orientation and pillars in the [0001] orientation, an increase in yield stress qualitatively observed experimentally between pillars oriented for basal and pyramidal slip. To explain this anisotropy in the yield stress between both orientations, it is necessary to account for two competing effects, namely, the Peierls stress, τ_o, and the CRSS of the weakest dislocation sources, τ_s [59]. The resolved shear stress at yield for the $[0001]$ orientation is observed to be on the order of the Peierls stress of $\langle c+a \rangle$ dislocations on 2nd order pyramidal planes. However, for the $[1122]$ orientation the resolved shear stress at yield is 50 times higher than the Peierls stress for $\langle a \rangle$ dislocations on the basal plane. According to the dislocation source model [29, 30], the CRSS of a dislocation source having a mean length of 800*b* is τ_s = 24.5 MPa, which is considerably higher than the Peierls stress for $\langle a \rangle$ dislocations on the basal plane and considerably lower than that for $\langle c+a \rangle$ dislocations on 2nd order pyramidal planes. Thus, it may be concluded that the yield stress always satisfies the condition that τ_y is always on the order of the maximum of τ_s and τ_o.

The dislocation density evolution as a function of axial engineering-strain for microcrystals having edge length D = 1 μm in both orientations is shown in Figure 5b. It is observed that the dislocation activities are predominantly on 2nd order pyramidal planes for $[0001]$ microcrystals, and predominantly on basal planes for $[1122]$ microcrystals. The Schmid factor on the basal plane is identically zero for loading along the $[0001]$ direction. Thus, in the absence of any friction stresses on the top surface of the microcrystal, no major dislocation slip is expected on the basal planes and plasticity is mediated entirely by ⟨*c+a*⟩ dislocations slip. As a result, the $[0001]$ microcrystals will deform in a multi-slip mode as shown in Figure 6b. On the other hand, while the maximum Schmid factor on the basal plane is 0.5 and on the 2nd order pyramidal planes is 0.3 for loading along the $[1122]$ direction, plasticity is mediated entirely by ⟨*a*⟩ dislocations slip on basal planes since the Peierls stress of dislocations on the 2nd order pyramidal planes is 200 times higher than that for dislocations on the basal planes. This ensures that no dislocation slip on 2nd order pyramidal planes is expected as shown in Figure 5b. Consequently, $[1122]$ oriented crystals will deform in a single slip mode as shown in Figure 6c.

The $[0001]$ microcrystals are observed to demonstrate a much stronger hardening response than $[1122]$ microcrystals. As discussed earlier, microcrystals with Schmid Factors favorable for basal slip deform in a single slip mode and subsequently the number of junctions forming during deformation is considerably small (if any) as shown in Figure 5a. Thus, no forest hardening is expected leading to a negligible hardening for the stress-strain curve. For $[0001]$ microcrystals, dislocation activities are predominantly on 2nd order pyramidal planes. Unlike basal planes, 2nd order pyramidal planes intersect one another and there is a high chance for active dislocations to be trapped by other active dislocations lying on intersecting 2nd order pyramidal planes. Following the discussion of the [0001] compression experiments, this will lead to the shutdown of active sources and a higher stress is needed to activate new sources. In response, a stronger hardening is observed for $[0001]$ microcrystals. This type of hardening has been first observed in FCC microcrystals and was termed “exhaustion hardening” [60].

In the case of an imposed shear stress on the top surface to mimic friction between the microcrystal top-surface and the indenter head, the resolved shear stress on the basal planes will constantly increase with increasing strain due to crystallographic rotations. At yield, θ_{mis} = 0°, and the resolved shear stress of all 2nd order pyramidal planes is the same. Thus, the microcrystal will initially deform in a multi-slip mode. With increasing strain, θ_{mis} increases and the resolved shear stress on a single 2nd order pyramidal plane becomes higher than others, leading to slip predominately on that single plane as shown in Figure 6a. When θ_{mis} reaches ~5° (i.e. at a strain of 1% in the current simulations), the resolved shear stress on the basal plane becomes large enough to activate ⟨a⟩ dislocations. Once this occurs, basal slip dominates and the dislocation density of ⟨a⟩-dislocation rapidly increases as shown in Figures 5b. This behavior

was also observed in [0001] compression experiments that displayed shear offsets nearly-perpendicular to the loading axis corresponding to the activation of basal slip, as shown in Figure 3c. In contrast to simulations, basal slip was not always the dominate deformation mechanisms observed experimentally with strain bursts seen accompanying stable hardening in these samples.

4.4. Dependence of yield stress on pillar diameter in experiments and simulations

Figure 7a shows the compressive yield stresses resolved onto the appropriate slip system as a function of sample diameter for each studied slip orientation in AZ31: (1) basal and (2) 2nd order pyramidal as well as resolved yield stresses at $\varepsilon = 0.65\%$ as predicted from the current 3D-DDD simulations of Mg for compression along the $[1122]$ and [0001] directions. This plot conveys that the yield stress increases with decreasing pillar diameter for each orientation, similar to the well-known size effect in strength for FCC and BCC single crystalline metallic nano-sized samples [23,61].

Experimental results on pure Mg [21–23] are also shown for comparison. Specifically, Ye et al. [21] reported the resolved yield stresses for basal slip in pure Mg, Byer et al. reported the stress at 4% strain [22], and Kim reported the resolved shear stresses at 2% strain [23]. A clear power-law size-dependence of the form $\tau \propto D^{-n}$ is observed for all orientations. However, the power law exponent for samples oriented for basal slip (n = –1.11 from experiments and n = –1.44 from simulations) is considerably higher than that for samples compressed along the c-axis (n = –0.36 from experiments and *n* = –0.34 from simulations). Micropillar compression experiments on pure Mg also showed a decrease in strengthening exponent for samples that deformed by 2nd order pyramidal slip compared to basal slip [22,23]. The flow stresses of both slip systems in AZ31 and simulated $[1122]$ pillars are similar to those reported for pure Mg [21–23].The slight variation between the predicted power-law exponent and the stress levels from [0001] DDD simulations and experiments is due to differences in the initial dislocation densities [33], and/or the strain level at which the flow stress is computed [34]. The experimentally-measured dislocation density reported experimentally equal to 1.1×10^{13} m^{-2} [10], which is almost twice the density in the current DDD simulations.

While Figure 7a suggests that the microcrystal orientation plays a role in the extent of observed size-effects on the strength of the crystal, the underlying source leading to such orientation influence is still unknown. Schneider, et al. attributed different size effect intensities of FCC and BCC to the different Peierls stresses τ_0 [62], which is strongly orientation dependent in HCP materials. According to the dislocation source model [62,63],

$$\tau_{CRSS} = \tau_0 + \alpha \frac{Gb}{\lambda_{max}},$$

we can see there are four important parameters: τ_0, *G*, *b* and λ_{max}. The main size dependent parameter is the statistically maximum dislocation source length, λ_{max}, while the other three are material properties and all orientation dependent due to material anisotropy. We can speculate that both the shear modulus, *G* and the Burgers vector magnitude, *b* contribute to the size dependence in addition to the Peierls stress, τ_0. In order to isolate such an effect due to anisotropy, we introduced an effective resolved shear stress per unit Burgers vector $\frac{\tau_{CRSS}-\tau_0}{Gb} = \frac{\alpha}{\lambda_{max}}$ to see the orientation influence on $\frac{\alpha}{\lambda_{max}}$. Figure 7b shows a clear power-law size-dependence for both orientations with the exponent being qualitatively the same. This suggests that the effect of orientation on size-induced strengthening shown in Figure 7a is from the material anisotropy, which is characterized by τ_0, *G*, and *b* [59,60].

To investigate the influence of orientation on the microstructural contribution to the size effect, we analyzed the microstructure evolution generated through the present DDD simulations. Figure 8 shows the superposition of several snapshots of dislocation microstructures separated by 0.2% strain intervals after yielding, in which the dislocation slip traces can be seen. Figure 8a conveys that almost all ⟨*c+a*⟩ dislocation sources were activated after yielding in the $[0001]$ oriented microcrystals since the Schmid factor is the same on all planes. For $[1122]$ oriented microcrystals, Figure 8b shows many ⟨*a*⟩ sources that were not activated. The figure also shows the presence of multiple straight screw dislocation segments. This dislocation evolution is likely a result of the low mobility of screw dislocations. In the case of $[1122]$ orientation ⟨*a*⟩ dislocation having Burgers vector in the $[1120]$ direction are easily activated since their Schmid factor is higher than ⟨*a*⟩ dislocations with the Burgers vectors parallel to $[1210]$ and $[2110]$. As a result, about half of the dislocation sources on the basal plane can contribute to plastic deformation during $[1122]$ loading. Thus, in the current DDD simulations, while the initial dislocation density on the basal plane is twice than that on 2nd order pyramidal planes, the number of activated dislocation sources on the basal plane is almost the same as the number of sources on the 2nd order pyramidal plane. This might explain why there is no orientation influence on the size effects, as shown in Figure 7b.

4.5. Dispersion/Solute effect

All previous experimental data on AZ31 has been reported for polycrystalline samples, making it difficult to separate the alloying effect on the strength from other microstructural effects. Akhtar and Teghtsoonian studied the CRSS for basal slip in several bulk single crystalline binary Mg alloys in tension [10,11,64]. These authors observed a CRSS of 2.9 MPa for basal slip in dilute Mg alloys with ~1.63 at.% Al and of 1.75 MPa in alloys with ~0.45% at.% Zn. These stresses are a factor of 3 higher than 0.5 MPa reported for basal slip in pure Mg [10,64] under similar processing treatments. They noted that for dilute concentrations, the increase in stress

caused by solid solution strengthening was proportional to $c^{\frac{2}{3}}$ where *c* is the atomic concentration of solute. Yasi, et al. used first principles computations to calculate the strengthening effect for slip in pure Mg across the basal plane by introducing solute particles of varying element [65]. Based on these calculations, we would expect a total solid-solution strengthening effect in AZ31 to be on the order of ~5 MPa. This predicted solid solution strengthening in bulk is much less than the predicted increase in flow stress due to the size effect.

The effect of secondary phases on the strength of nano-sized metallic samples has not been extensively studied. The yield strength was reported to be independent of pillar size in a Ni-based alloy (Inconel MA6000) that contained 20-30 nm diameter Y_2O_3 particles spaced less than 100 nm apart [66]. The length-scale of particle spacing dominated the sample size and so they observed bulk-like behavior. Fe nanopillars with low initial dislocation densities that contained Nb clusters exhibited a slight increase in strength of ~ 0.11GPa, as compared to pure Fe nanopillars but this was considered statistically insignificant compared to the overall strength of 2 GPa [67]. These authors concluded that the strengthening was governed by intrinsic properties and not by the presence of precipitates.

The spacing of 2nd phases observed in this work was as great as 675 nm, greater than the radius of most compression samples, and so we would expect the stress required to activate single-arm sources to be on the order or greater than the bowing stress. Figure 7a clearly shows that there is no significant contribution to the yield stress from the presence of 2nd phases as the alloy shows similar yield stresses as Mg. Sub-micron samples show a post-elastic insensitivity to the presence of 2nd phases, but further study is required to determine whether they contribute to the rate of hardening in the 2 and 5 μm diameter samples.

5. Conclusion

We investigated the mechanical response of AZ31 nanopillars compressed along two crystallographic directions: (1) parallel to the (0001) direction, nominally oriented for basal slip and (2) misoriented from the c-axis by 22-69°. We also employed 3D-DDD simulations for pure Mg pillars under $[11\bar{2}2]$ and [0001] compressive loading. For samples nominally oriented for basal slip, we observed stress-strain behavior indicative of single-slip deformation and strain bursts typical of nano-compression experiments. DDD simulations revealed weak dislocation interactions resulting in weak hardening and single slip. Samples compressed along the c-axis displayed both strain bursts and significant hardening in their stress-strain data. DDD simulations showed a pronounced increase in junction formation due to the activation of multiple intersecting slip systems. Yield strengths in these samples were approximately twice as great as basal samples and were high enough to activate basal slip even for small misalignments away from the c-axis. There is a clear size effect seen in each set of samples, the yield strength

increasing with decreasing pillar diameter. The size effect followed a power-law with differing exponent for each system that was shown to be a result of the underlying anisotropic intrinsic lattice resistance. The power-law exponent for basal slip was -1.11 for experiments and -1.44 for simulations while the exponent for samples compressed along the c-axis was -0.36 for experiments and -0.34 for simulations. By accounting for the anisotropic material properties through the effective resolved shear stress per unit burgers vector, this anisotropy disappeared showing that the mechanism of the size effect is the same in both orientations. Yield strengths in the AZ31 alloy were similar to Mg in both orientations showing that at this length scale, the size effect overrides solid solution strengthening and that the yield strength is insensitive to the presence of second phases.

Acknowledgements

Research was sponsored by the Army Research Laboratory and was accomplished under Cooperative Agreement Number W911NF-12-2-0022. The views and conclusions contained in this document are those of the authors and should not be interpreted as representing the official policies, either expressed or implied, of the Army Research Laboratory or the U.S. Government. The U.S. Government is authorized to reproduce and distribute reprints for Government purposes notwithstanding any copyright notation herein. Authors ZHA and JRG also gratefully acknowledge the financial support of NSF (DMR-1204864). The authors also acknowledge the facilities and staff of the Kavli Nanoscience Institute at Caltech. The authors thank Dongchan Jang and Carol Garland for TEM assistance.

References

[1] Dix EH. SAE Tech Pap 1929:498.

[2] Archbutt SL, Jenkin JW. Nature 1922;109:251.

[3] Luo A. JOM 2002;54:42.

[4] Staiger MP, Pietak AM, Huadmai J, Dias G. Biomaterials 2006;27:1728.

[5] Kulekci MK. Int J Adv Manuf Technol 2007;39:851.

[6] Zeng R, Dietzel W, Witte F, Hort N, Blawert C. Adv Eng Mater 2008;10:B3.

[7] Ogarevic VV, Stephens RI. Annu Rev Mater Sci 1990;20:141.

[8] Mordlike BL, Ebert T. Mater Sci Eng A 2001;302:37.

[9] Mises R V. ZAMM - Zeitschrift für Angew Math und Mech 1928;8:161.

[10] Akhtar A, Teghtsoonian E. Acta Metall 1969;17:1339.

[11] Akhtar A, Teghtsoonian E. Acta Metall 1969;17:1351.

[12] Bohlen J, Nürnberg MR, Senn JW, Letzig D, Agnew SR. Acta Mater 2007;55:2101.

[13] Barnett MR, Keshavarz Z, Beer a G, Atwell D. Acta Mater 2004;52:5093.

[14] Ding SX, Lee WT, Chang CP, Chang LW, Kao PW. Scr Mater 2008;59:1006.

[15] Uchic MD, Shade P a., Dimiduk DM. Annu Rev Mater Res 2009;39:361.

[16] Greer JR, De Hosson JTM. Prog Mater Sci 2011;56:654.

[17] Schneider AS, Kiener D, Yakacki CM, Maier HJ, Gruber PA, Tamura N, Kunz M, Minor AM, Frick CP. Mater Sci Eng A 2013;559:147.

[18] El-Awady JA, Uchic MD, Shade PA, Kim S-L, Rao SI, Dimiduk DM, Woodward C. Scr Mater 2013;68:207.

[19] Byer CM, Li B, Cao B, Ramesh KT. Scr Mater 2010;62:536.

[20] Lilleodden E. Scr Mater 2010;62:532.

[21] Ye J, Mishra RK, Sachdev AK, Minor AM. Scr Mater 2011;64:292.

[22] Byer CM, Ramesh KT. Acta Mater 2013;61:3808.

[23] Kim GS. Small Volume Investigation of Slip and Twinning in Magnesium Single Crystals. 2011.

[24] Kim GS, Yi S, Huang Y, Lilleodden E. MRS Proc 2011;1224:1224.

[25] Yu Q, Qi L, Chen K, Mishra RK, Li J, Minor AM. Nano Lett 2012;12:887.

[26] Zbib HM, Diaz de la Rubia T. Int J Plast 2002;18:1133.

[27] Zbib HM, Rhee M, Hirth JP. Int J Mech Sci 1998;40:113.

[28] Pérez-Prado MT, Ruano O a. Scr Mater 2002;46:149.

[29] Greer JR, Nix WD. Phys Rev B 2006;73:1.

[30] Ng K, Ngan A. Acta Mater 2008;56:1712.

[31] Greer JR, Oliver WC, Nix WD. Acta Mater 2005;53:1821.

[32] Volkert C a., Lilleodden ET. Philos Mag 2006;86:5567.

[33] Shan ZW, Mishra RK, Syed Asif S, Warren OL, Minor AM. Nat Mater 2008;7:115.

[34] Wang Y., Huang J. Mater Chem Phys 2003;81:11.

[35] Partridge PG. Int Mater Rev 1967;12:169.

[36] Balasubramanian S, Anand L. Acta Mater 2002;50:133.

[37] Conrad H, Robertson WD. Trans Metall Soc Aime 1957;209:503.

[38] Reed-Hill R., Robertson W. Acta Metall 1957;5:717.

[39] Staroselsky A, Anand L. Int J Plast 2003;19:1843.

[40] Groh S, Marin EB, Horstemeyer MF, Bammann DJ. Model Simul Mater Sci Eng 2009;17:075009.

[41] Tang Y, El-Awady JA. Mater Sci Eng A 2014;618:424.

[42] Fan H, Li Z, Huang M. Scr Mater 2012;66:813.

[43] Capolungo L. Acta Mater 2011;59:2909.

[44] Tang Y, El-Awady JA. Acta Mater 2014;71:319.

[45] Kuroda M. Acta Mater 2013;61:2283.

[46] Shade PA, Wheeler R, Choi YS, Uchic MD, Dimiduk DM, Fraser HL. Acta Mater 2009;57:4580.

[47] Hearmon RF. The Elastic Constants of Crystals and Other Anisoptropic Materials. Berlin: Springer-Verlag; 1979.

[48] Nikishin a. V., Nikolaev DI. Crystallogr Reports 2008;53:493.

[49] Tromans D. 2011;6:462.

[50] Masoumi M, Zarandi F, Pekguleryuz M. Mater Sci … 2011;528:1268.

[51] Stanford N, Atwell D. Metall Mater Trans A 2013;44:4830.

[52] Nakaura Y, Watanabe A, Ohori K. Mater Trans 2006;47:1743.

[53] Brinckmann S, Kim J-Y, Greer J. Phys Rev Lett 2008;100:155502.

[54] Dimiduk D, Uchic MD, Parthasarathy TA. Acta Mater 2005;53:4065.

[55] Obara T, Yoshinga H, Morozumi S. Acta Metall 1973;21:845.

[56] Yoshinaga H, Horiuchi R. Trans JIM 1963;4:1.

[57] Barnett MR. Mater Sci Eng A 2007;464:1.

[58] Wang C, Zhang H-Y, Wang H-Y, Liu G-J, Jiang Q-C. Scr Mater 2013;69:445.

[59] El-Awady JA, Wen M, Ghoniem NM. J Mech Phys Solids 2009;57:32.

[60] Rao SI, Dimiduk DM, Parthasarathy TA, Uchic MD, Tang M, Woodward C. Acta Mater 2008;56:3245.

[61] Uchic MD, Dimiduk DM, Florando JN, Nix WD. Science 2004;305:986.

[62] Schneider AS, Frick CP, Clark BG, Gruber PA, Arzt E. Mater Sci Eng A 2011;528:1540.

[63] Parthasarathy T a., Rao SI, Dimiduk DM, Uchic MD, Trinkle DR. Scr Mater 2007;56:313.

[64] Akhtar A, Teghtsoonian E. Philos Mag 1972;25:897.

[65] Yasi J a., Hector LG, Trinkle DR. Acta Mater 2010;58:5704.

[66] Girault B, Schneider AS, Frick CP, Arzt E. Adv Eng Mater 2010;12:385.

[67] Xie KY, Shrestha S, Cao Y, Felfer PJ, Wang Y, Liao X, Cairney JM, Ringer SP. Acta Mater 2013;61:439.

Figure Captions

Figure 1. (a) TEM micrograph showing a porous oxide covering the AZ31 surface. This was observed during electro-polishing at elevated temperatures or if the sample was not immediately cleaned following polishing. The amorphous layer of Pt was used as protection during the TEM sample preparation process. (b) SEM image of the smoothed sample surface following electro-polishing. Al-Mg precipitates ranging approximately 1 to 10 μm can be seen partially and fully embedded in the AZ31 matrix. (c) Orientation Imaging Microscopy map generated by EBSD showing grain structure of annealed and polished surface with average grain size of 11.5±9.6 μm. (d) Stereographic triangle showing the grain orientations that were used to fabricate compression samples.

Figure 2. (a) Engineering stress strain data for 847 nm and 2125 nm basal sample. Data for the 850 nm samples displays frequent strain bursts characteristic of similar micro- and nano-compression experiments. No significant work hardening is seen up to 15%. The 2100 nm sample shows significant hardening and smaller burst magnitude. (b) Post-deformation SEM image of 850 nm samples showing deformation is accommodated by a set of parallel slip planes. (c) Post-deformation SEM image of 2100 nm sample showing deformation is also accommodated by a set of parallel slip planes. (d) TEM micrograph showing a slip plane taken from a sample oriented for basal slip. The inset diffraction pattern shows that these slip planes are basal planes. TEM images courtesy of Dongchan Jang.

Figure 3. (a) Pre-deformation SEM image of 840 nm diameter sample nominally oriented for compression parallel to the c-axis. (b) Engineering stress-strain data for pyramidal sample displaying strain bursts and significant strain hardening. (c) Post-deformation SEM image showing deformation is mostly homogeneous. A single slip plane that is nearly perpendicular to the loading axis can be seen towards the bottom of the pillar. Samples greater than a micron in diameter failed by catastrophic strain bursts and so no comparison of the post-elastic behavior can be made to sub-micron samples. (d) Post-deformation TEM micrograph of a 860 nm-diameter c-axis sample. Diffraction contrast indicates a high dislocation density. The inset diffraction spot pattern shows that the sample is single crystalline.

Figure 4. (a) TEM micrograph of bulk AZ31. Inset shows diffraction spot pattern for the image. Several cylindrical and spherical particles can be seen. The white foam-like structures are surface oxidation that began forming on the highly reactive Mg. (b) A HRTEM image of one of the particles of ~15 nm in diameter. Moire fringes indicate the presence of a second phase. (c) EDS data reveals the particles to be Mn-rich. TEM images courtesy of Carol Garland.

Figure 5. (a) Engineering-stress and number of junction nodes versus engineering-strain for microcrystals having 1 μm diameter and compressed along the [0001] and $[11\bar{2}2]$ directions, respectively. (b) The total dislocation density, the $\langle a \rangle$ dislocation density on basal planes, and $\langle c+a \rangle$ dislocation density on the 2nd order pyramidal planes versus the axial engineering-strain.

Figure 6. Effective plastic strain map and deformation shape at 1.5% strain for compression along: (a) $[0001]$ with 0-10° misorientation, (b) $[0001]$ without misorientation and (c) $[1122]$ microcrystals. Note that the misorientation is achieved by applying shear stress on the top surface (see text). The displacement field in the *x* direction is magnified 5 times.

Figure 7. (a) CRSS for compression samples oriented for basal and pyramidal slip plot versus sample diameter. Included are reported yield strengths for similar micro- and nano-pillar compression experiments on pure Mg. The alloy pillars show a greater rate of strengthening than pure Mg. Both sets of experimental samples and simulation of $[1122]$ compression show similar yield strengths to pure Mg. (b) The effective resolved shear stress per unit burgers vector plot versus sample diameter for the same set of data shown in (a). All data except simulated [0001] compression, is seen to collapse showing that the size effect is the same for both basal and pyramidal slip.

Figure 8. Dislocation microstructure evolution shown sequentially for (a) [0001] microcrystals between 0% and 0.6% strain; and (b) $[1122]$ microcrystals between 0%, and 0.4%. The notation of the <*a*> $<\bar{1}120>$ dislocations is used in (b).

Table 1. Slip planes and Burgers vectors used in the present DD framework [34].

Slip planes	Basal – {0001}	Prismatic – $\{\bar{1}010\}$		1st Order Pyramidal – $\{\bar{1}011\}$		2nd Order Pyramidal II – $\{\bar{1}122\}$
Burgers vectors	$\langle a\rangle \equiv \frac{1}{3}<\bar{1}120>$	$\langle a\rangle \equiv \frac{1}{3}<\bar{1}120>$	$\langle c\rangle \equiv \langle 0001\rangle$	$\langle a\rangle \equiv \frac{1}{3}<\bar{1}120>$	$\langle c+a\rangle \equiv \frac{1}{3}<\bar{1}123>$	$\langle c+a\rangle \equiv \frac{1}{3}<\bar{1}123>$

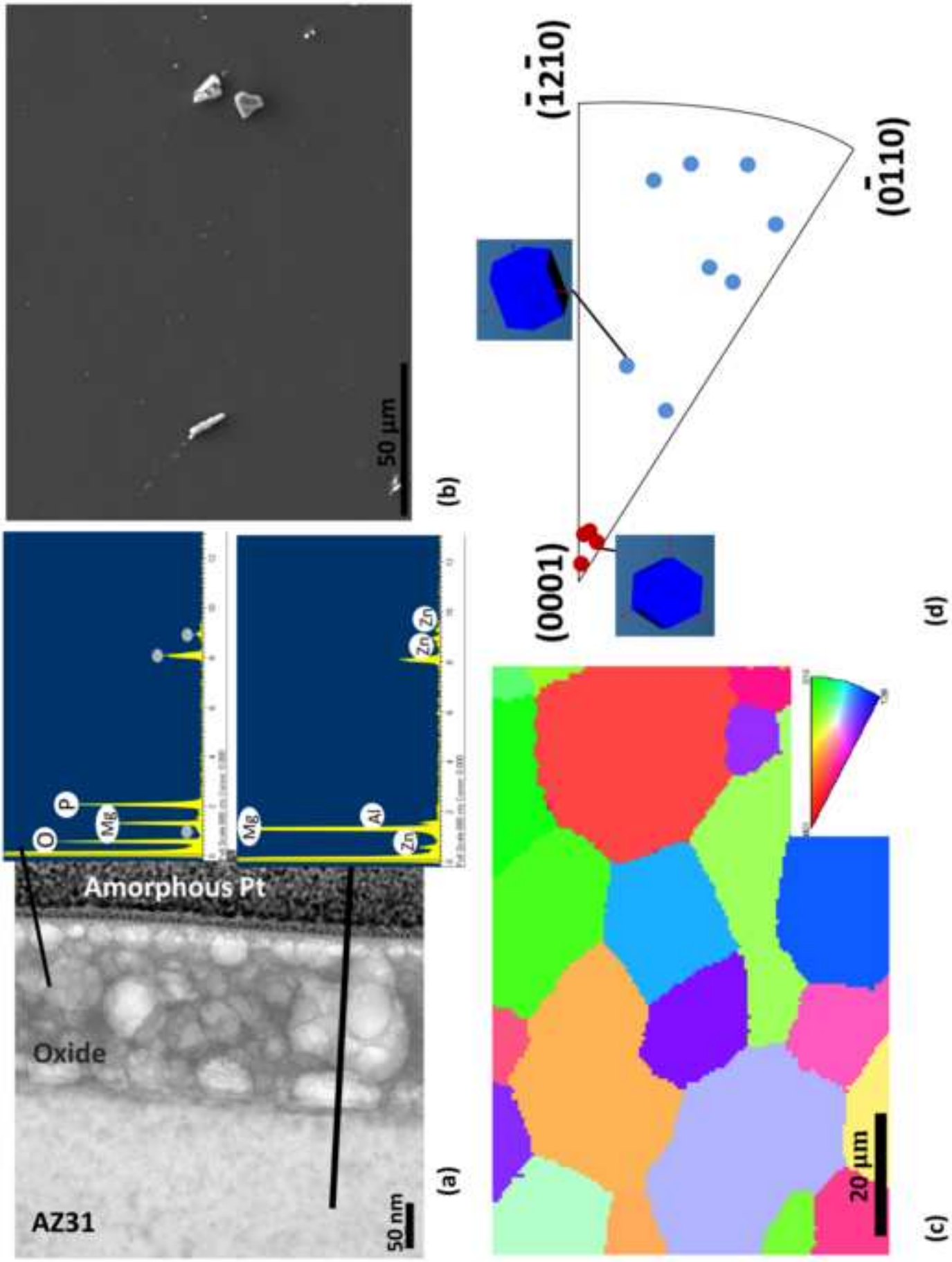
Amorphous Pt
Oxide
AZ31
50 nm
O
P
Mg
Mg
Al
Zn
Zn
Zn
(a)
50 µm
(b)
20 µm
(c)
(0001)
(1210)
(0110)
(d)

Figure1

Figure2

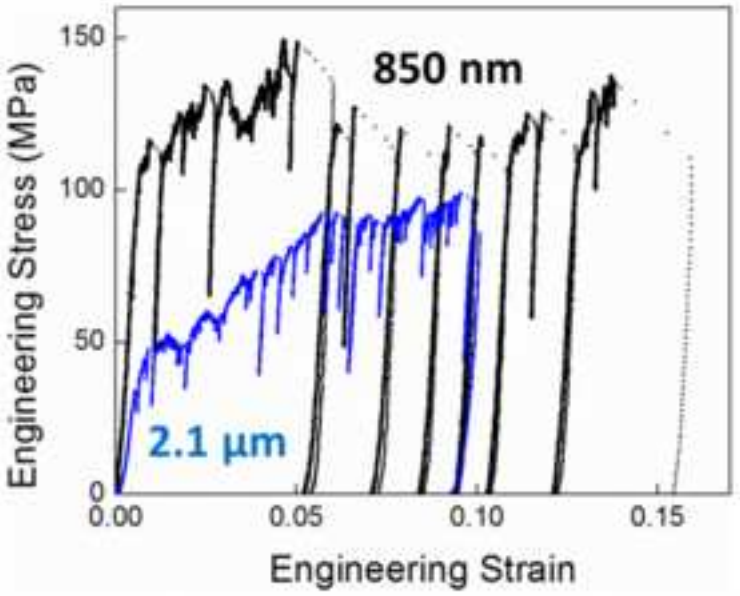

(a)

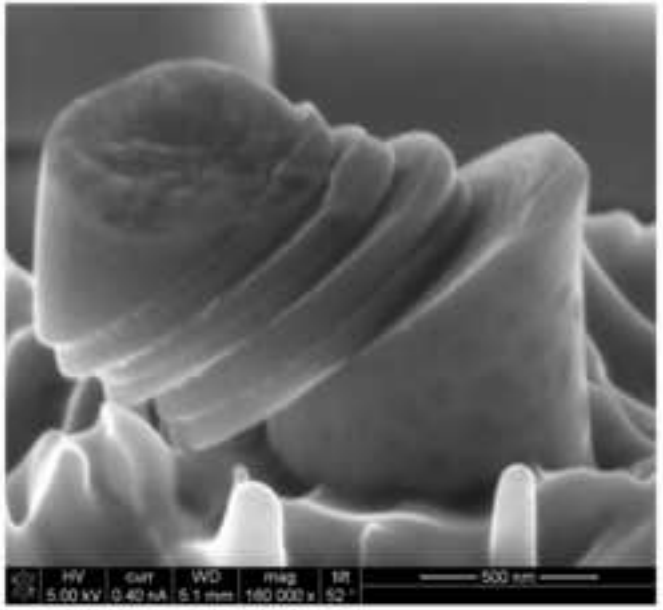

(b)

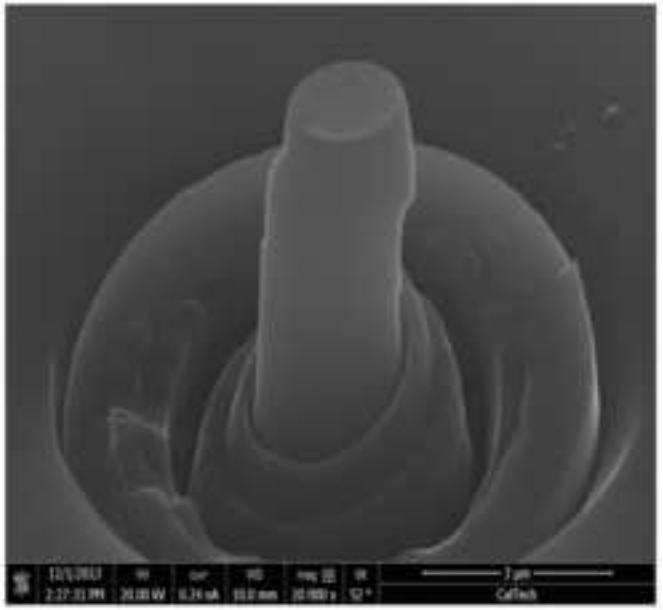

(c)

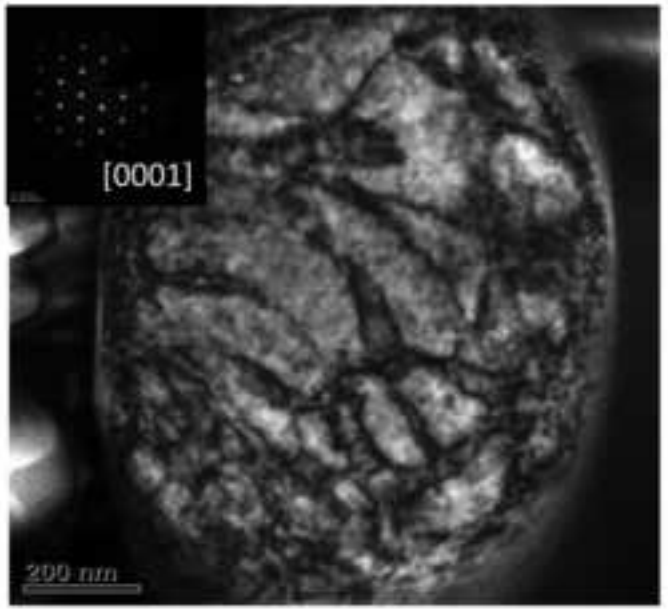

(d)

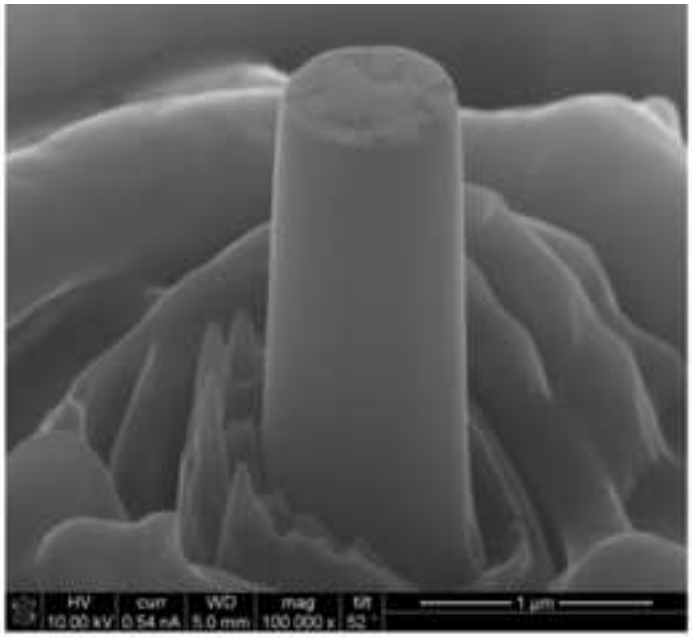

(a)

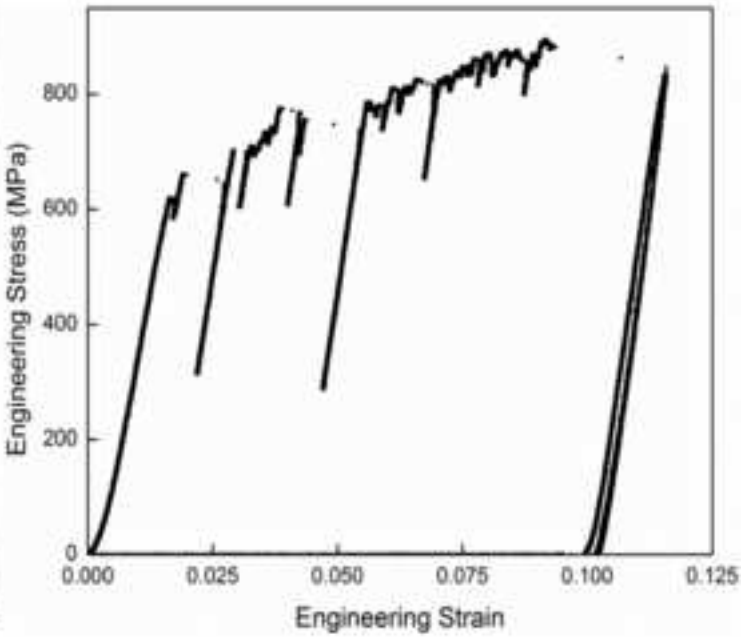

(b)

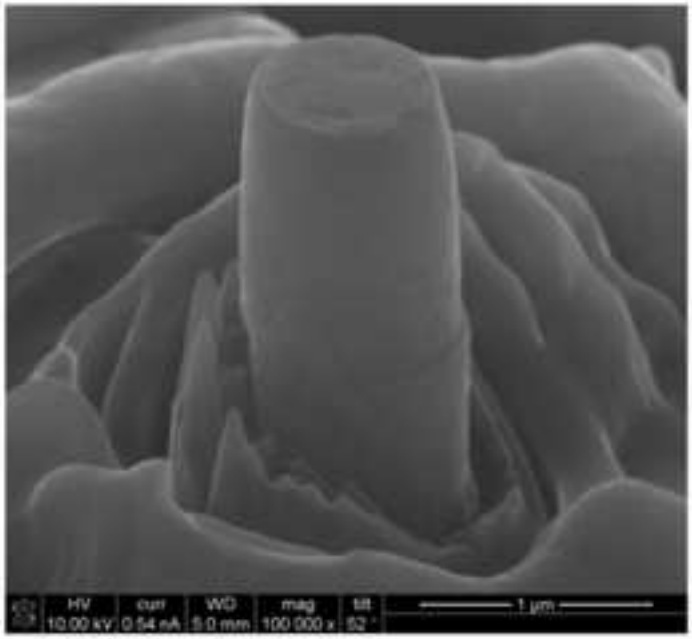

(c)

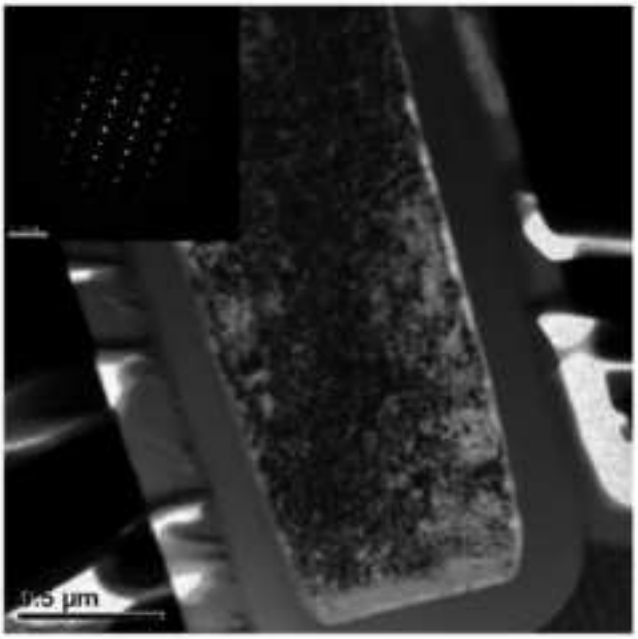

(d)

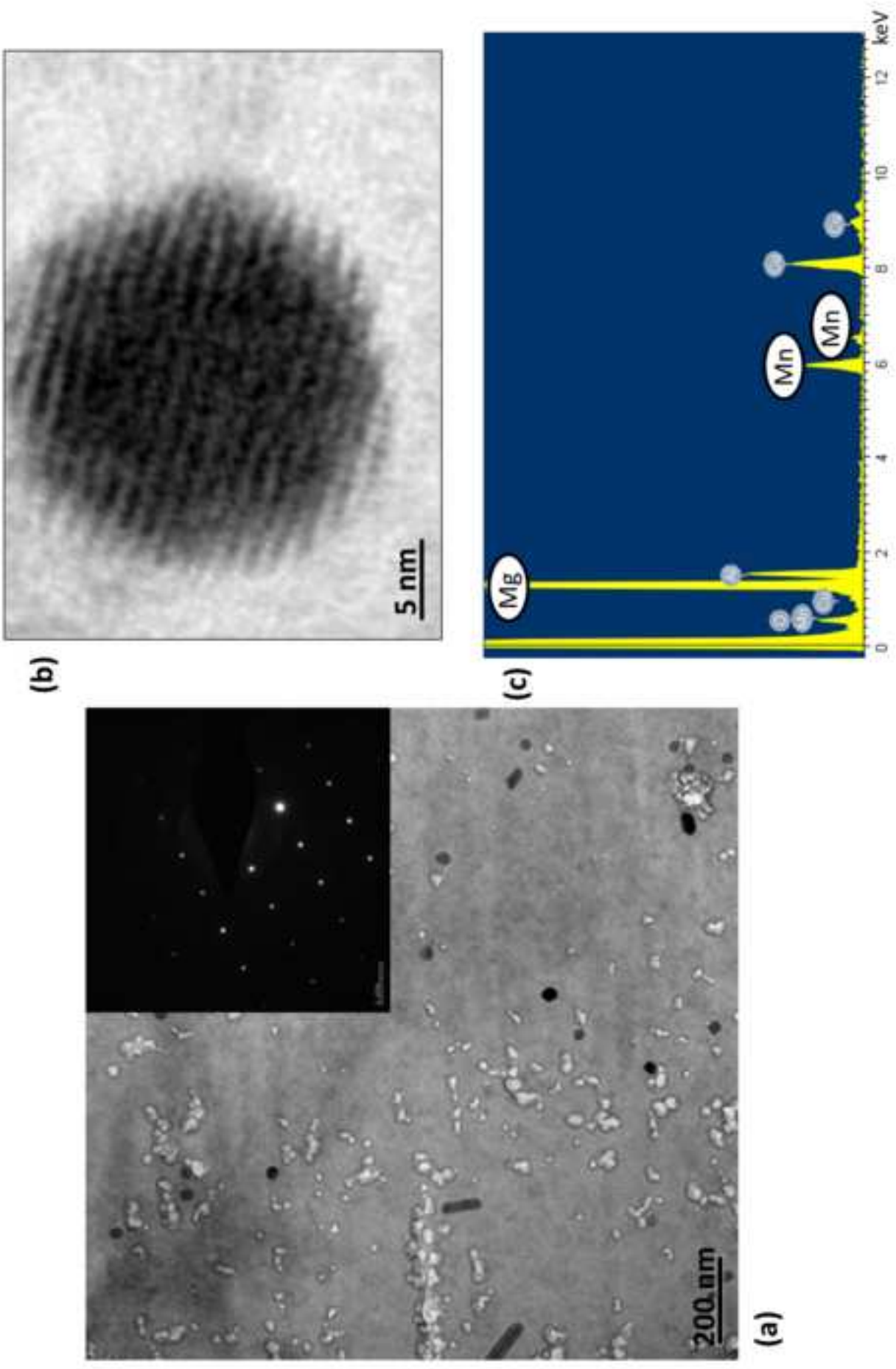

Figure4

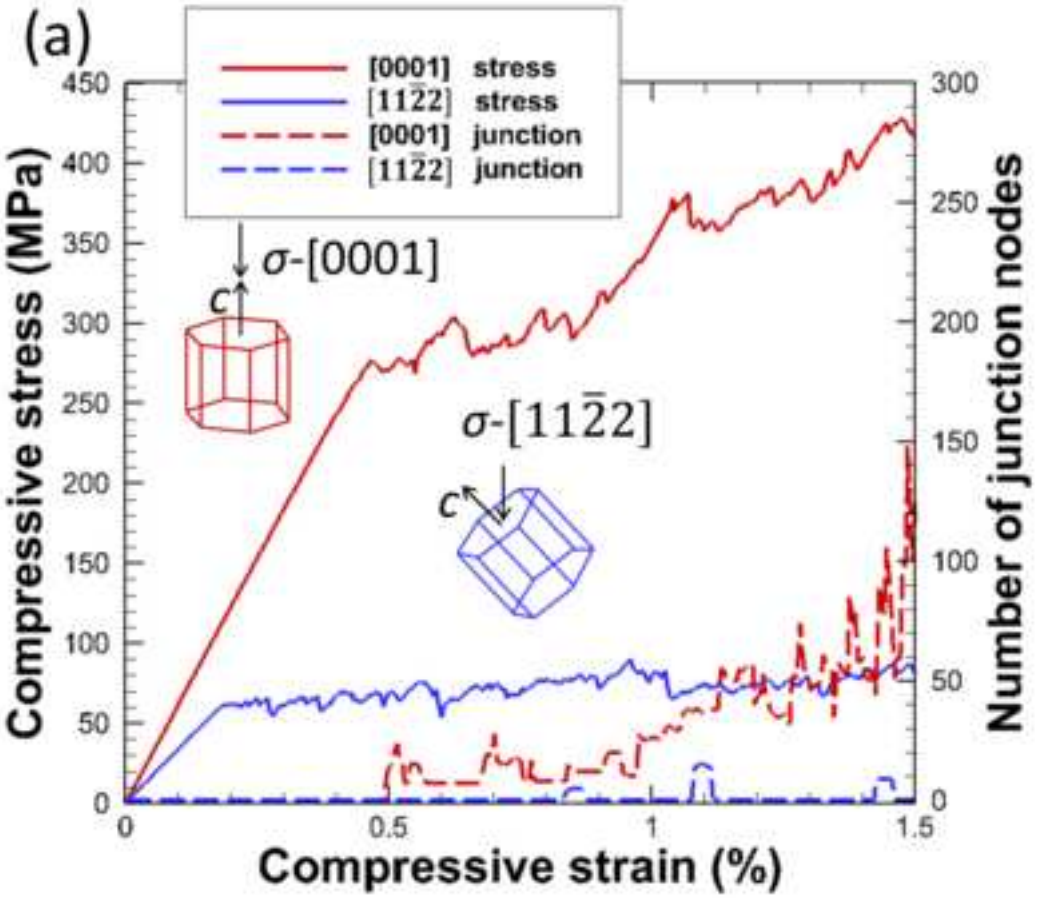

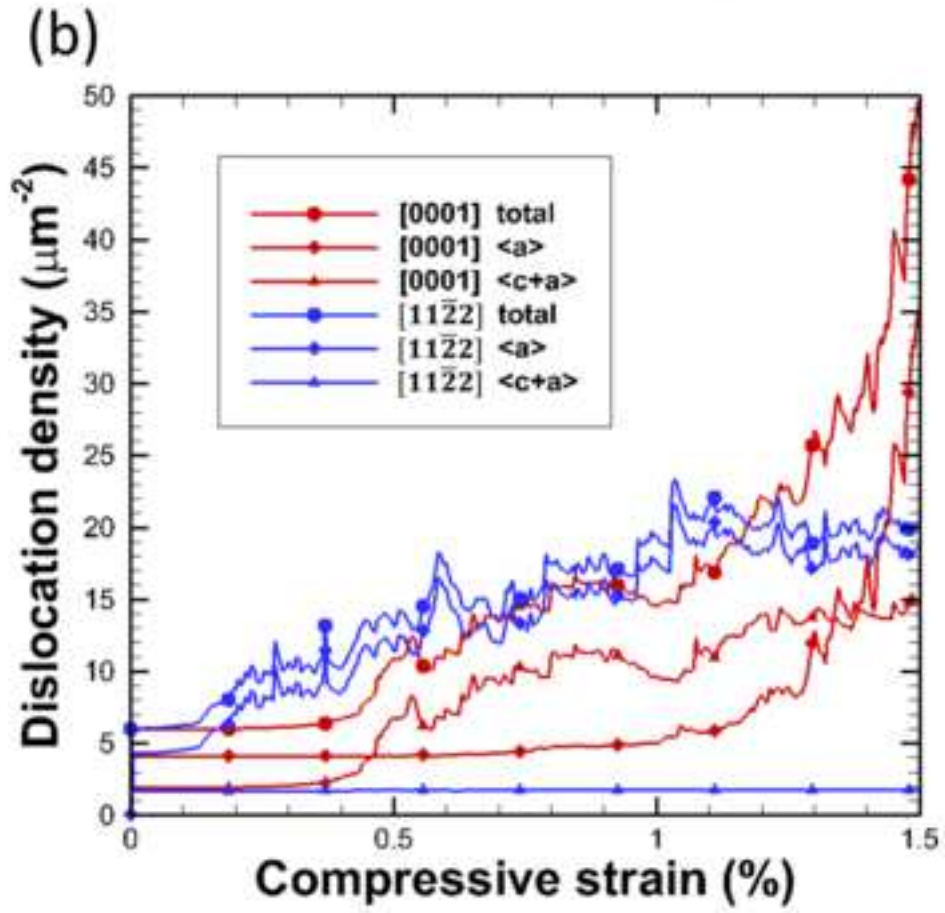

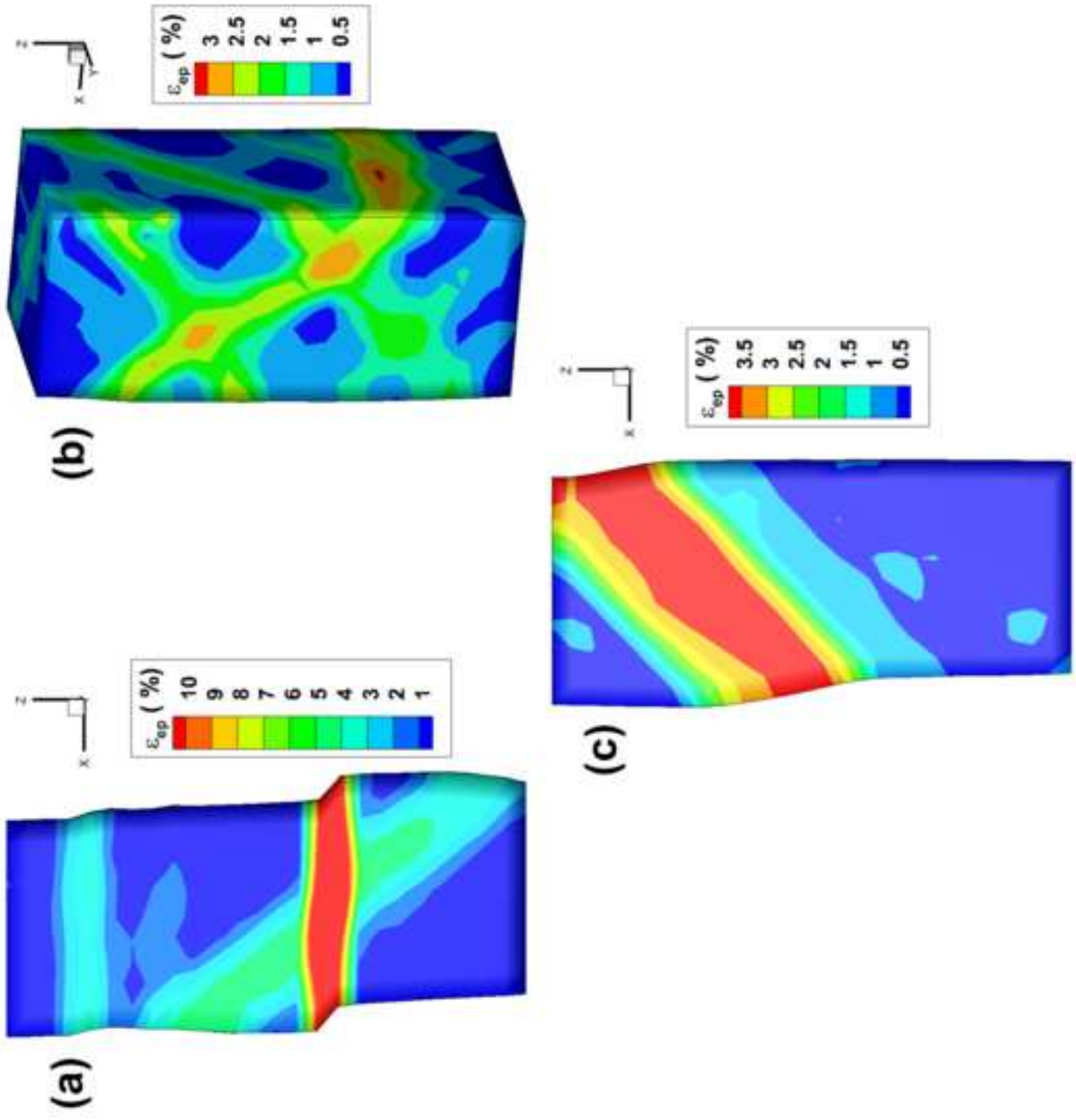
(a)
ε_{ep} (%)
10
9
8
7
6
5
4
3
2
1
Z
X
(b)
ε_{ep} (%)
3
2.5
2
1.5
1
0.5
Z
Y
X
(c)
ε_{ep} (%)
3.5
3
2.5
2
1.5
1
0.5
Z
X

Figure6

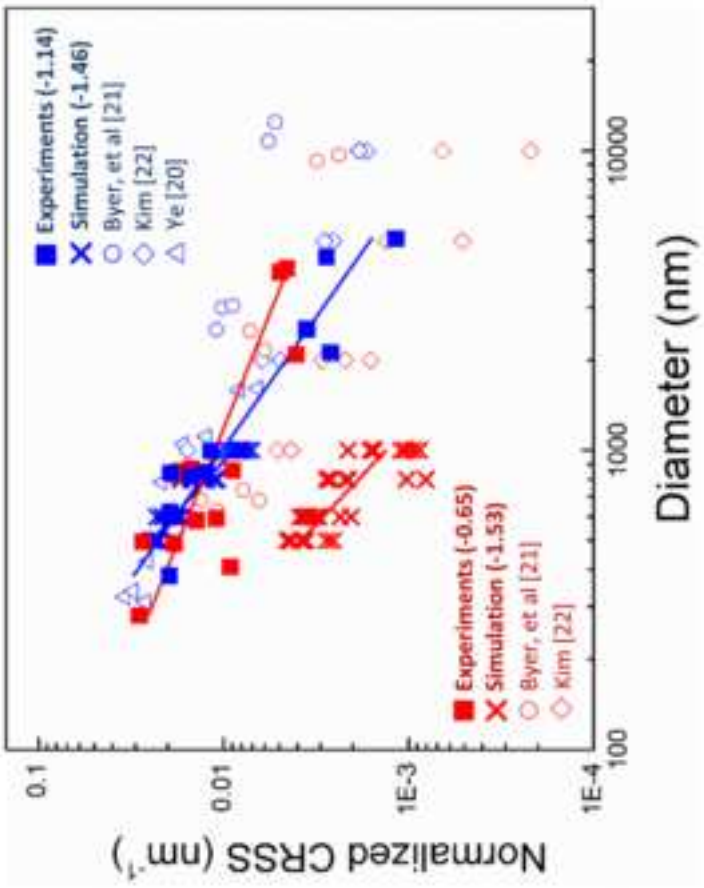
Experiments (-1.14)
Simulation (-1.46)
Byer, et al [21]
Kim [22]
Ye [20]
Experiments (-0.65)
Simulation (-1.53)
Byer, et al [21]
Kim [22]
Normalized CRSS (nm^{-1})
0.1
0.01
1E-3
1E-4
100
1000
10000
Diameter (nm)
(b)

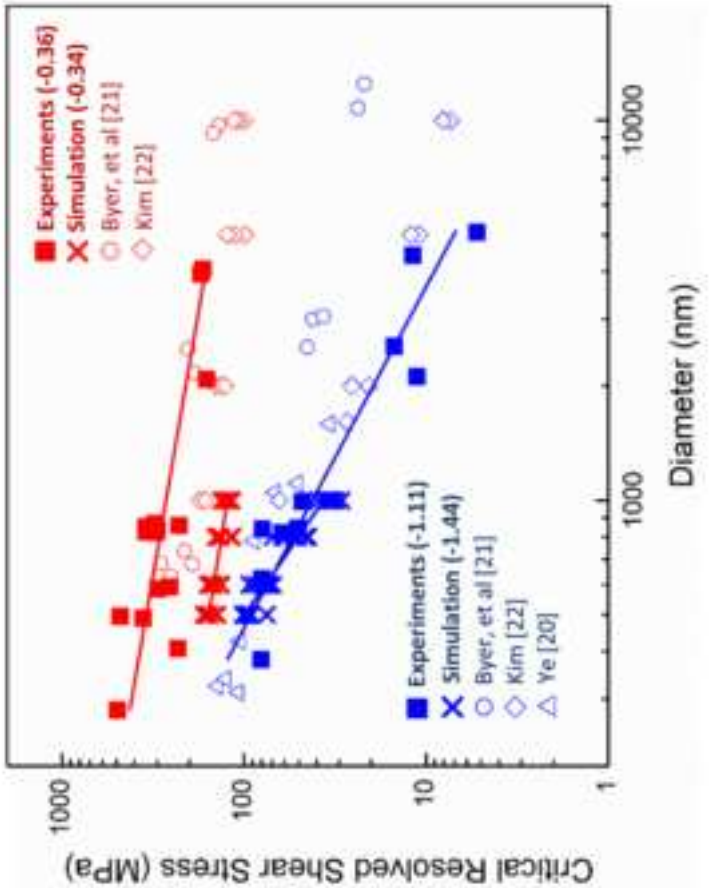
Experiments (-0.36)
Simulation (-0.34)
Byer, et al [21]
Kim [22]
Experiments (-1.11)
Simulation (-1.44)
Byer, et al [21]
Kim [22]
Ye [20]
Critical Resolved Shear Stress (MPa)
1000
100
10
1
100
1000
10000
Diameter (nm)
(a)

Figure7

Figure8